ARTICLE   **Open Access**

Simultaneous photocatalytic degradation and SERS detection of tetracycline with self-sustainable and recyclable ternary PI/TiO₂/Ag flexible microfibers

Donglai Han[1]✉, Boyang Guo[1], Yanru Li[1], Wei Feng[1], Keyan Liu[1], Tianna Wu[2], Yuchun Wan[1], Lili Wang[2], Ming Gao[3], Yang Liu[3], Lili Yang[3], Maobin Wei[3]✉ and Shuo Yang[2]✉

Abstract

Facile and efficient photocatalysts using sunlight, as well as fast and sensitive surface-enhanced Raman spectroscopy (SERS) substrates, are urgently needed for practical degradation of tetracycline (TC). To meet these requirements, a new paradigm for PI/TiO₂/Ag organic–inorganic ternary flexible microfibers based on semiconducting titanium dioxide (TiO₂), the noble metal silver (Ag) and the conjugated polymer polyimide (PI) was developed by engineering a simple method. Under sunlight, the photocatalytic characteristics of the PI/TiO₂/Ag flexible microfibers containing varying amounts of Ag quantum dots (QDs) were evaluated with photocatalytic degradation of TC in aqueous solution. The results demonstrated that the amount of Ag affected the photocatalytic activity. Among the tested samples, PI/TiO₂/Ag-0.07 (93.1%) exhibited a higher photocatalytic degradation rate than PI/TiO₂ (25.7%), PI/TiO₂/Ag-0.05 (77.7%), and PI/TiO₂/Ag-0.09 (63.3%). This observation and evaluation conducted in the present work strongly indicated a charge transfer mechanism. Moreover, the PI/TiO₂/Ag-0.07 flexible microfibers exhibited highly sensitive SERS detection, as demonstrated by the observation of the Raman peaks for TC even at an extremely low concentration of 10^{-10} moles per liter. The excellent photocatalytic performance and SERS detection capability of the PI/TiO₂/Ag flexible microfibers arose from the Schottky barrier formed between Ag and TiO₂ and also from the outstanding plasmonic resonance and visible light absorptivity of Ag, along with immobilization by the PI. The successful synthesis of PI/TiO₂/Ag flexible microfibers holds significant promise for sensitive detection and efficient photocatalytic degradation of antibiotics.

Introduction

TC has emerged as one of the most extensively employed antibiotics due to its simple synthesis, low cost, excellent antibacterial properties, and broad applicability, and it is used in treating human diseases and as a growth promoter in the livestock and aquaculture industries[1]. However, TC is a continuous antibiotic that is neither fully absorbed by living creatures nor eliminated via traditional water treatment. Untreated TC seriously impairs human health and the ecological balance[2], so finding a method for effective detection and elimination of TC residues is crucial.

SERS is a spectroscopic detection technique that allows simple, rapid, and sensitive determination of the spectra of target analytes based on interactions between Raman substrates and target analytes during illumination[3]. Photocatalysis is a green technology that relies on the ability of photocatalysts to decompose pollutants under irradiation without generating resource waste[4]. TiO₂ is one of the most extensively studied materials in the field of photocatalysis, primarily due to its nontoxicity, cost-effectiveness, high efficiency, high oxidation capacity, photostability and

Correspondence: Donglai Han (DLHan_1015@163.com) or
Maobin Wei (jlsdzccw@126.com) or Shuo Yang (yangshuo_2011@163.com)
[1]School of Materials Science and Engineering, Changchun University of Science and Technology, 130022 Changchun, China
[2]College of Science, Changchun University, 130022 Changchun, China
Full list of author information is available at the end of the article

relatively high chemical stability[5]. Even more surprising is that TiO$_2$ exhibits high Raman activity[6]. However, the wide bandgap and easy recombination of charge carriers in TiO$_2$ limit its use in photocatalysis[7], and the chemical enhancement mechanism of Raman is not sufficient to meet the requirements of sensitive detection[6]. To overcome these drawbacks of TiO$_2$, heterojunctions composed of TiO$_2$ and other noble metals have been investigated, for example, by combining TiO$_2$ with gold, silver, nickel, or platinum[8–10]. Among various noble metals, Ag was used to form a composite material with TiO$_2$ due to its strong surface plasmon resonance (SPR) absorption and significant charge capture in the visible spectrum[11,12]. This approach utilizes the visible light absorptivity of Ag to extend the absorption range and enhance the efficiency of sunlight utilization and maximizes the use of Ag plasmonic resonance and the Schottky barrier formed at the Ag-TiO$_2$ interface to inhibit recombination of the photogenerated charge carriers and enhance charge resonance transfer[13]. Consequently, it significantly enhances photocatalytic degradation and SERS detection. However, it should be noted that TiO$_2$/Ag composite materials are mostly powders, which can easily cause secondary pollution and are not conducive to subsequent recycling[11,12]. The most common approaches used to address these issues involve loading the powdered samples onto magnetic carriers, ITO, and silicon dioxide[14–16]. Beyond that, organic flexible nanofibers prepared by electrospinning have also served as carriers to immobilize TiO$_2$/Ag powders, enhance recyclability and prevent secondary pollution[17]. PI is one of the most commonly utilized organic flexible nanofibers, owing to its remarkable flexibility, large specific surface area and high porosity[18]. The incorporation of TiO$_2$/Ag into PI would enhance the dispersion of TiO$_2$/Ag and improve its photocatalytic and SERS performance while enabling recycling and mitigating the risk of secondary pollution[19].

In the present work, we developed a facile approach for the fabrication of PI/TiO$_2$/Ag organic−inorganic ternary flexible microfibers exhibiting sensitive SERS detection and efficient photocatalytic degradation of TC under simulated sunlight. The photocatalytic capabilities of the PI/TiO$_2$ and PI/TiO$_2$/Ag flexible microfibers were assessed under simulated solar light via degradation of TC as a model compound. The SERS detection efficiency of the PI/TiO$_2$/Ag-0.07 flexible microfibers was evaluated with 4-aminophenol (4-ATP) and TC. The structural characteristics of the PI/TiO$_2$/Ag flexible microfibers and the role of the Ag QDs in enhancing the photocatalytic and SERS activity of PI/TiO$_2$ are the focus of the present study and discussion.

Results and discussion
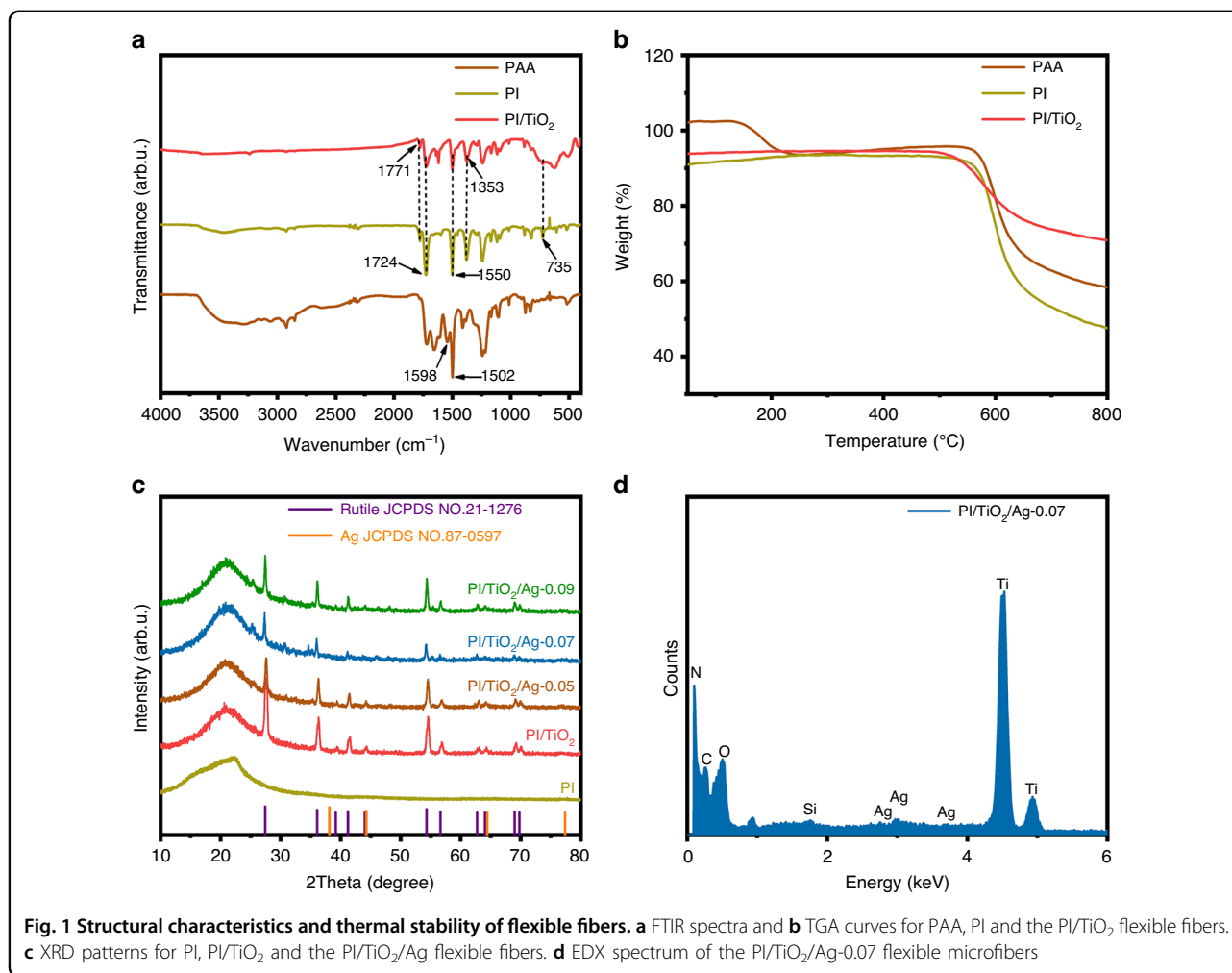### Structural and morphological characterization
The structural and morphological features of PI, PI/TiO$_2$ and the PI/TiO$_2$/Ag flexible nano/microfibers were studied with several analytical techniques, including Fourier transform infrared spectroscopy (FTIR), thermogravimetric analysis (TGA), X-ray diffraction (XRD), energy dispersive X-ray spectroscopy (EDX), scanning electron microscopy (SEM), transmission electron microscopy (TEM) and X-ray photoelectron spectroscopy (XPS).

FT-IR spectroscopy was used to determine structures and chemical bonds of the polyamide acid (PAA), PI, and PI/TiO$_2$ flexible fibers. As exhibited in Fig. 1a, the absorption peaks at 1598 and 1502 cm^{-1} were attributed to the C $=$ O stretching vibration and N–H vibration of PAA[20]. The absorption peaks at 1771, 1724, 1550, 1353, and 735 cm^{-1} were associated with asymmetric stretching and symmetric stretching vibrations of aromatic C $=$ N bonds in the triazine unit, stretching vibrations of C–N–C moieties in the five-membered imide rings and bending vibrations of the C $=$ O bonds in PI, respectively[21]. The broad peaks at 400 to 800 cm^{-1} represented Ti–O–Ti stretching vibrations, which confirmed in situ surface growth of TiO$_2$ on the PI[22]. These findings indicate that the primary chemical structure and bonding of the PI remained unaffected by TiO$_2$ deposition.

The thermal stabilities were investigated with TGA. As shown in Fig. 1b, the imidization reaction of PAA began at approximately 200 °C. As the temperature reached 300 °C, the macromolecular chains within the PAA nanofibers underwent rearrangement to a more stable conformation and ultimately formed PI nanofibers. Based on the thermal weight loss curves for PAA and the PI nanofibers at 300 °C, the PI nanofibers no longer exhibited thermal weight losses, and hence, there was no imidization reaction. From that, we inferred that after 2 h of thermal imidization of the PAA nanofibers at 300 °C, the internal molecular chains of PI adopted stable conformations and showed good thermal stability. At approximately 580 °C, an obvious inflection appeared because the molecular chains of the PI nanofibers began to break. At this point, the thermal weight loss rate reached a maximum due to carbonization of the PI nanofibers. At approximately 800 °C, they are almost fully converted into carbon fibers[19]. Notably, the weight loss from PI/TiO$_2$ is less than that from PI, which was ascribed to the addition of TiO$_2$. These results showed that our prepared PI and PI/TiO$_2$ nanofibers were thermally stable.

The generated samples were subjected to XRD analyses to investigate their crystal structures and phase transitions. Figure 1c depicts the XRD patterns for PI, PI/TiO$_2$ and the PI/TiO$_2$/Ag flexible fibers. The prominent peak at 2θ $=$ 27.9° was related to the interlayer π-π stacking of PI, specifically corresponding to the (001) facet of PI[23]. The primary diffraction peaks for PI/TiO$_2$ and PI/TiO$_2$/Ag were comparable. The typical diffraction peaks at 27.4°, 36.1°, 39.2°, 41.2°, 44.1°, 54.3°, 56.6°, 62.7°, 64.0°, 69.0° and 69.8°

Fig. 1 Structural characteristics and thermal stability of flexible fibers. **a** FTIR spectra and **b** TGA curves for PAA, PI and the PI/TiO₂ flexible fibers. **c** XRD patterns for PI, PI/TiO₂ and the PI/TiO₂/Ag flexible fibers. **d** EDX spectrum of the PI/TiO₂/Ag-0.07 flexible microfibers

were attributed to crystalline rutile TiO (JCPDS NO. 21-1276)[24]. However, oddly, the XRD patterns for PI/TiO₂/Ag exhibited no diffraction peaks for Ag. This may be explained by the low amount of Ag present or by the fact that the diffraction peaks for the Ag QDs were obscured by those of TiO₂. Nevertheless, the EDX spectrum of PI/TiO₂/Ag-0.07 confirmed the presence of Ag. As shown in Fig. 1d, Ag, Ti, O, C and N were detected. The aforementioned results demonstrated the formation of PI/TiO₂/Ag.

The morphologies of PAA, PI, PI/TiO₂ and PI/TiO₂/Ag were examined with SEM. As illustrated in Fig. 2a, b, the PAA and PI nanofibers exhibited smooth and uniform surfaces. However, the diameters of the PI nanofibers (approximately 200 nm) were smaller than those of the PAA nanofibers (approximately 250 nm). This was due to volatilization of the DMF solvent and the thermal imidization reactions occurring during calcination. As seen from Fig. 2c, TiO₂ nanorods (NRs) with petal-like shapes were uniformly grown on the surfaces of the PI nanofibers. However, the Ag QDs were not readily visible in Fig. 2d–f.

Furthermore, the microstructures of PI/TiO₂ and PI/TiO₂/Ag were investigated with TEM and high-resolution TEM (HRTEM). Figure 3(a1–d1) confirms that in PI/TiO₂, TiO₂ nanorods (size: approximately 250 nm) were uniformly and compactly grown on the surfaces of the PI nanofibers. Figure 3a2–d2 also shows that the number of Ag DQs on the surface of PI/TiO₂ gradually increased with increasing concentrations of AgNO₃. Figure 3a3–d3 demonstrates that Ag DQs were bonded to PI/TiO₂ and exhibited an average size of 15 ± 5 nm, and the PI/TiO₂/Ag samples included both TiO₂ NR and Ag DQ crystals. The lattice spacing of 0.32 nm observed in the figure matched that of the (110) crystal plane of TiO₂ (JCPDS NO. 21-1276)[25]. The lattice distance of 0.24 nm in the figure corresponded to the (111) crystal plane of Ag (JCPDS NO. 87-0597)[26]. The elemental maps for the PI/TiO₂/Ag-0.07 microfibers are depicted in Fig. 3e, which indicates that the C, O, N, Ti and Ag elements were well distributed throughout the PI/TiO₂ nanofibers. Additionally, the distribution diameters of C and N in PI were smaller than that of Ti in TiO₂, and the distribution
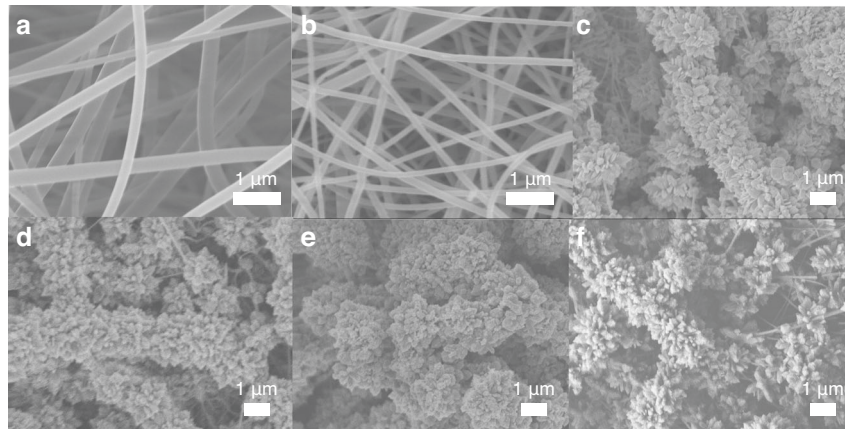
Fig. 2 Surface morphology of flexible fibers. SEM images of **a** PAA, **b** PI, **c** PI/TiO$_2$, **d** PI/TiO$_2$/Ag-0.05, **e** PI/TiO$_2$/Ag-0.07 and **f** PI/TiO$_2$/Ag-0.09 flexible fibers
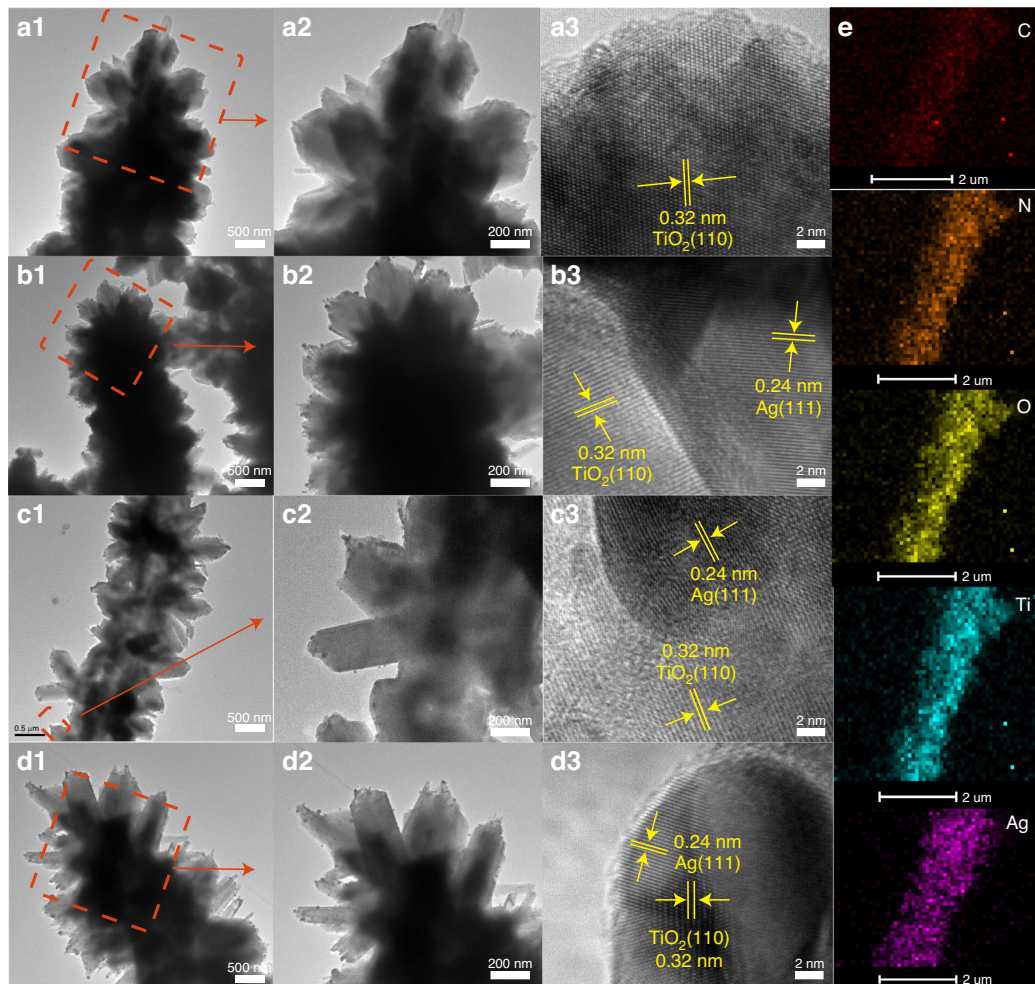

Fig. 3 Microstructure and element distribution of flexible fibers. TEM and HRTEM images of **a** PI/TiO$_2$, **b** PI/TiO$_2$/Ag-0.05, **c** PI/TiO$_2$/Ag-0.07 and **d** PI/TiO$_2$/Ag-0.09 flexible microfibers. **e** EDX element maps for C, N, O, Ti and Ag in the PI/TiO$_2$/Ag-0.07 flexible microfibers

diameter of Ti in TiO_2 was smaller than that of Ag, indicating the formation of a hierarchical core-shell structure.

Furthermore, the valence states and elemental compositions of the prepared samples were verified with XPS analyses. As observed in Fig. 4a, the peaks for C, N and O in PI/TiO_2 and $PI/TiO_2/Ag$ were consistent with those for PI. The peaks observed in Fig. 4b with binding energies of 458.5 eV and 464.2 eV were assigned to Ti $2p_{3/2}$ and Ti $2p_{1/2}$, and the 5.7 eV splitting between them indicated the presence of Ti^{4+}[27]. The Ag 3d XPS spectrum of $PI/TiO_2/$ Ag-0.07 is shown in Fig. 4c. The peaks at 368.7 eV and 374.7 eV indicated the $3d_{5/2}$ and $3d_{3/2}$ states of metallic Ag (0), respectively. Notably, the energy difference of 6.0 eV between the Ag $3d_{3/2}$ and Ag $3d_{5/2}$ binding energies was characteristic of metallic Ag[28]. Figure 4d displays the C 1 s XPS data for PI, PI/TiO_2, and $PI/TiO_2/Ag$-0.07, which contained three peaks located at 288.2 eV, 285.8 eV, and 284.6 eV, respectively. The binding energies of these peaks were calibrated relative to the C 1s peak at 284.6 eV, which was assigned to carbon contamination or sp^2 C-C/ C = C bonds. In comparison, the peaks at 288.3 eV and 285.8 eV were attributed to the O−C = O bonds in the triazine rings and the C−N bonds in PI, respectively[29]. As shown in Fig. 4e, the N 1 s peak at 400.4 eV was associated with the N−(C)$_3$ bonds of PI[30]. In Fig. 4f, the O 1 s spectrum of PI displayed two peaks at 532.0 and 533.2 eV, which were attributed to C = O and C−O or adsorbed water, respectively. In comparison, PI/TiO_2 and $PI/TiO_2/$ Ag showed one additional peak at 529.8 eV, which corresponded to the Ti−O bonds[31,32]. Notably, in Fig. 4d–f, the peaks for PI/TiO_2 were redshifted relative to those for PI, and the peaks for $PI/TiO_2/Ag$ exhibited redshifts relative to those for PI/TiO_2, indicating successful incorporation of TiO_2 into PI, as well as PI, TiO_2, and Ag. In addition, the Ti 2p and O 1s binding energies for $PI/TiO_2/$ Ag were redshifted toward lower energy compared to those for PI/TiO_2, indicating electron transfer from Ag to TiO_2.

Photodegradation of TC

To ascertain the specific surface areas and pore structures of the synthesized photocatalysts, nitrogen adsorption-desorption isotherms were generated. As shown in Fig. 5a, the isotherms for PAA, PI, PI/TiO_2 and the $PI/TiO_2/Ag$ flexible fibers were all type IV isotherms with type H3 hysteresis loops, implying that slit-like mesoporous structures were formed. The specific surface areas for PAA, PI, PI/TiO_2 and the $PI/TiO_2/Ag$ flexible fibers were estimated to be 17, 17, 21, and 29 m^2/g, respectively. Clearly, the $PI/TiO_2/Ag$ flexible microfibers had the highest specific surface area. Figure 5b shows that a significant proportion of the pores had diameters ranging from 0 to 15 nm, which is consistent with the SEM

and TEM images. These abundant active sites in the hierarchical mesoporous nanostructure are believed to result in the high photocatalytic activity and facile photocatalytic reactions[33].

As seen in Fig. 5c, the photocatalytic capabilities of PI, PI/TiO_2 and the $PI/TiO_2/Ag$ flexible fibers with different amounts of Ag QD were investigated with photocatalytic degradation of TC under simulated sunlight. PI and PI/TiO_2 exhibited very poor catalytic performance in degrading TC (16.2% and 25.7% conversions after 120 min) due to inefficient photogenerated carrier separation and transfer. Then, we loaded Ag QDs on the PI/TiO_2 microfibers. As the content of $AgNO_3$ was increased from 0.05 M to 0.07 M, the photocatalytic efficiency for TC degradation increased from 77.7% to 93.1%. However, as the concentration of $AgNO_3$ was increased to 0.09 M, the photocatalytic degradation efficiency did not continue to increase but rather decreased to 63.3%. The enhanced photocatalytic efficiency was attributed to multiple factors[26]. First, the formation of a Schottky barrier between Ag and TiO_2 provided efficient separation of the photogenerated electrons and holes. Additionally, the remarkable SPR and visible light absorptivity of Ag enhanced the photocatalytic activity and solar energy utilization efficiency. Moreover, the immobilization capability of PI and incorporation of the Ag QDs resulted in a higher specific surface area, which also enhanced the photocatalytic efficiency. However, when more Ag QDs (0.09 M $AgNO_3$) were loaded, the excess Ag QDs tended to occupy some of the reactive sites, which inhibited the formation of photocatalytic intermediates and the adsorption of TC, and consequently reduced the photocatalytic performance[34,35]. Additionally, $PI/TiO_2/Ag$ was employed for degradation of Rhodamine B (Rh B), Methylene Blue (MB) and Methyl Orange (MO). As shown in Fig. 5d, $PI/TiO_2/Ag$ exhibited excellent photocatalytic degradation activity with these three pollutants (100%, 95.5%, and 100%), confirming its high efficiency as a versatile photocatalyst suitable for the removal of diverse pollutants.

Photoreduction mechanism of TC

The absorptivities and band gaps (E_g) of PI, PI/TiO_2 and the $PI/TiO_2/Ag$-0.07 flexible fibers were determined with ultraviolet−visible diffuse reflectance spectroscopy (UV−vis DRS) and the corresponding Tauc plots. In Fig. 6a, the absorption spectra of PI and PI/TiO_2 exhibited significant peaks in the UV region, and they decreased rapidly in the visible region. When the Ag QDs were deposited, as shown in the UV−vis DR spectrum of $PI/TiO_2/Ag$-0.07, absorption of visible wavelengths was greatly enhanced, which was attributed to SPR absorption by the Ag QDs[36]. The inserted plots in Fig. 6a depict the Tauc curves for PI,
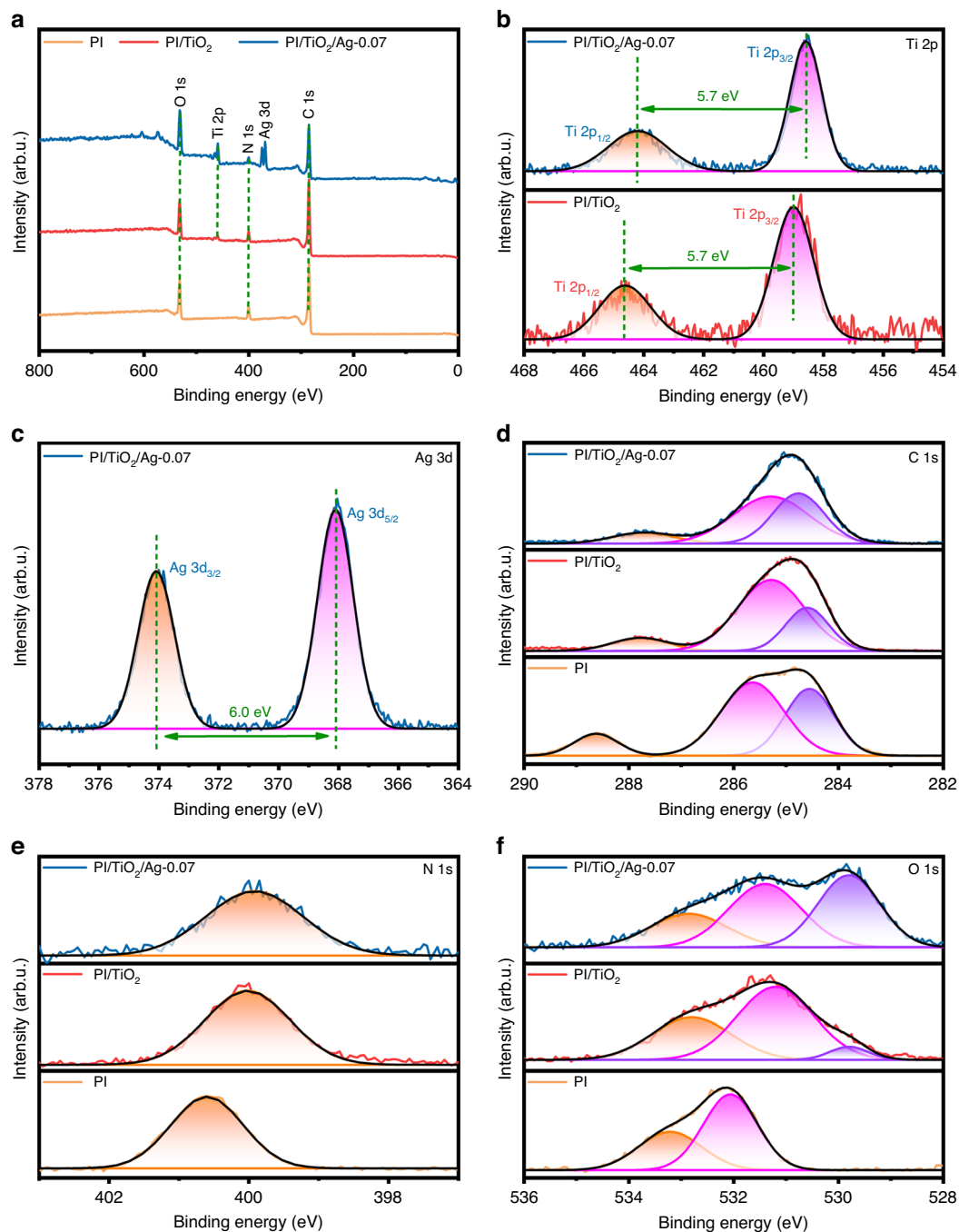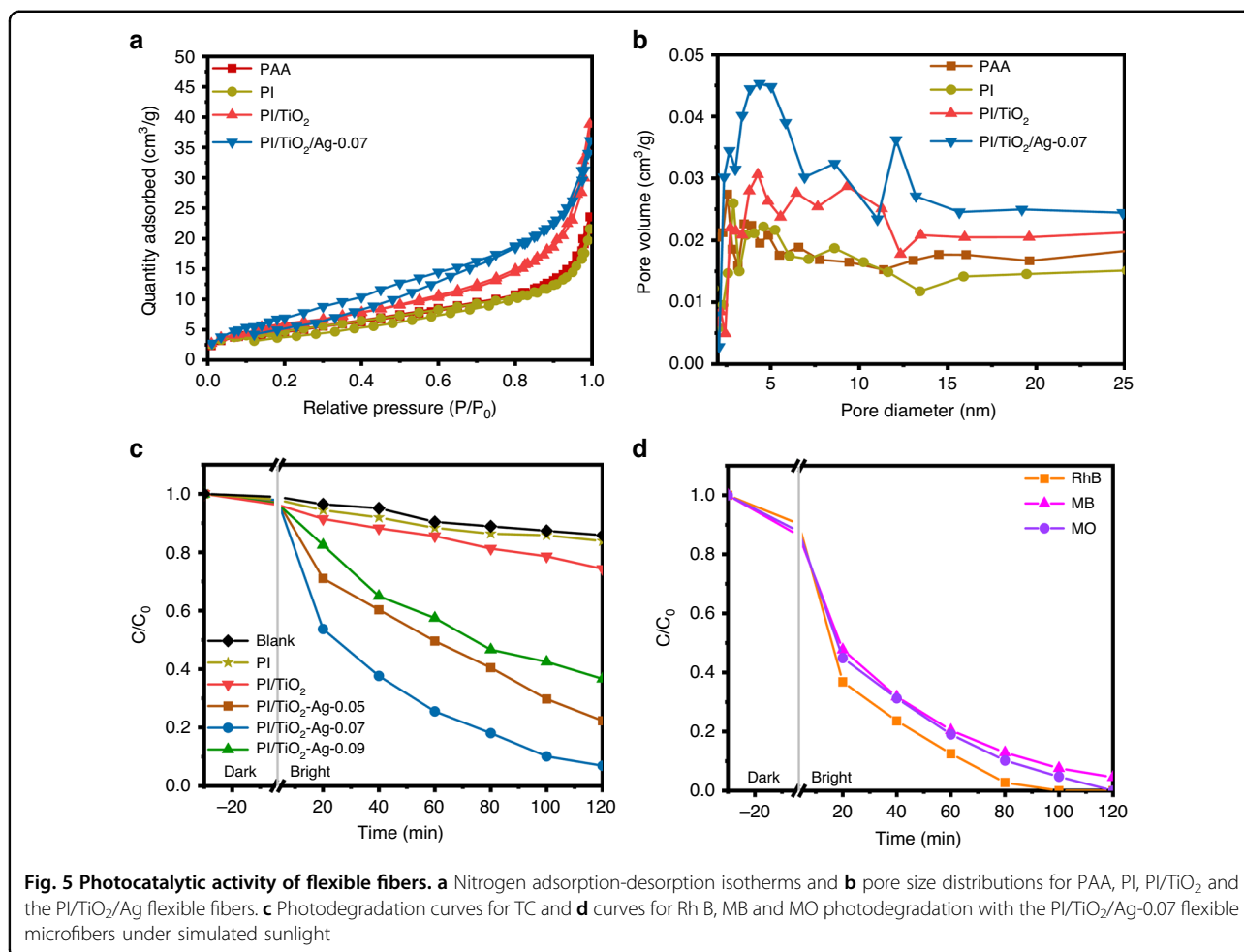
Fig. 4 Electronic states and chemical compositions of lexible fibers. XPS data for PI, PI/TiO$_2$ and the PI/TiO$_2$/Ag-0.07 flexible fibers: **a** full survey; **b** Ti 2p; **c** Ag 3d; **d** C 1s; **e** N 1s and **f** O 1s XPS data

PI/TiO$_2$ and PI/TiO$_2$/Ag-0.07. The graphs show that the E_g values were 2.59 eV, 2.96 eV and 2.14 eV.

The photocatalytic activity and separation of the photogenerated charge carriers in the obtained samples were evaluated with the photoluminescence (PL) spectra generated with an excitation wavelength of 350 nm and electrochemical impedance spectroscopy (EIS). As shown in

Fig. 6b, PI exhibited a prominent peak in the wavelength range 400–500 nm. Similar peaks for PI/TiO$_2$ and PI/TiO$_2$/Ag-0.07 were centered at approximately 410 nm. This was attributed to the fact that the Ag 3d orbitals accepted electrons and captured the charge carriers to inhibit recombination of the photogenerated electrons and holes[37,38]. Noticeably, the PL intensity of PI/TiO$_2$/Ag-0.07 was much

Fig. 5 Photocatalytic activity of flexible fibers. a Nitrogen adsorption-desorption isotherms and **b** pore size distributions for PAA, PI, PI/TiO$_2$ and the PI/TiO$_2$/Ag flexible fibers. **c** Photodegradation curves for TC and **d** curves for Rh B, MB and MO photodegradation with the PI/TiO$_2$/Ag-0.07 flexible microfibers under simulated sunlight

lower than that of PI/TiO$_2$, suggesting a reduced rate for electron-hole recombination and improved photocatalytic activity. In other words, the synergy of the Ag QDs and the TiO$_2$ NR interlayer facilitated transport of the photo-generated charge carriers. Here, we also note that charge transfer increased the photocatalytic efficiency of PI/TiO$_2$/Ag and also improved its SERS performance[39]. Figure 6c also shows Nyquist plots for various flexible nano/micro-fibers. The radius of the arc reflects the reaction rate at the surface of the flexible composite fiber, which can be inter-preted as the charge transfer resistance (Rct). It was dis-covered that PI/TiO$_2$/Ag-0.07 has a much smaller Rct than PI/TiO$_2$ and PI, revealing that the PI/TiO$_2$/Ag-0.07 flexible microfibers showed the highest efficiency in separating the photogenerated electron-hole pairs and facilitating rapid interfacial charge transfer[40].

Furthermore, photocurrent response (i-t) experiments were performed under simulated sunlight with on/off cycles of 20 s. As illustrated in Fig. 6d, the as-prepared samples exhibited fairly stable photocurrent responses. In particular, the PI/TiO$_2$/Ag-0.07 flexible microfibers

showed much higher photocurrents and transient pho-tocurrent densities than PI/TiO$_2$ and PI, indicating that PI/TiO$_2$/Ag-0.07 separated the photogenerated electrons most effectively. This enhanced performance was attrib-uted to effective interfacial charge transfer facilitated by the tight bonding and synergy of the TiO$_2$ NRs and Ag QDs. Furthermore, this unique combination contributed to the excellent photocatalytic and SERS activities of PI/TiO$_2$/Ag-0.07.

The semiconducting and flat band (Fermi energy level, E_F) potentials were determined via electrochemical Mott-Schottky (MS) tests. Figure 6e illustrates the potentials for PI, PI/TiO$_2$ and PI/TiO$_2$/Ag-0.07, which were 0.29 V, -1.31 V and -0.60 V (vs. Ag/AgCl), respectively. These values were referenced to the normal hydrogen electrode (NHE) potential with the following formula:

$$E_{NHE} = E_{Ag/AgCl} + 0.198V \qquad (1)$$

Thus, the calculated E_F potentials for PI, PI/TiO$_2$ and PI/TiO$_2$/Ag-0.07 were 0.49 V, -1.11 V and -0.40 V vs.
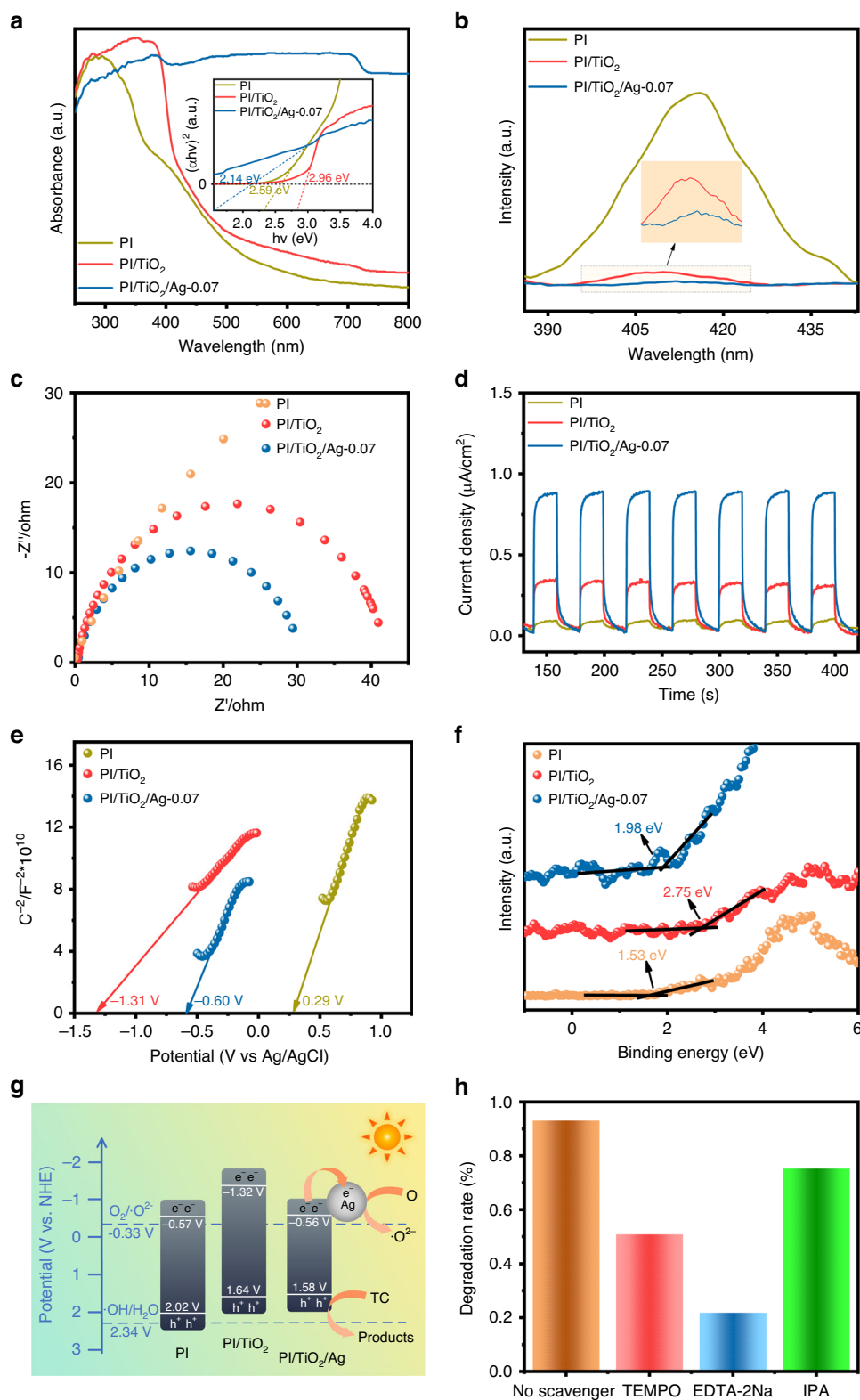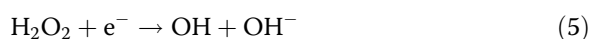
Fig. 6 Optical properties, electrochemical performance and photocatalytic machanism of flexible fibers. a Ultraviolet–visible diffuse reflectance spectra and Tauc plots, **b** PL, **c** EIS and **d** transient photocurrent response spectra, **e** Mott–Schottky curves, **f** VB-XPS spectra, **g** energetics for photocatalytic degradation of TC by PI, PI/TiO$_2$ and the PI/TiO$_2$/Ag-0.07 flexible fibers and **h** effects of different scavengers on the photocatalytic degradation of TC by the PI/TiO$_2$/Ag-0.07 flexible microfibers

NHE, respectively. Furthermore, the VB-XPS spectra (Fig. 6f) were used to determine the relative potentials of the valence bands (VB) vs. the Fermi energy level, and the estimated values for PI, PI/TiO$_2$, and PI/TiO$_2$/Ag-0.07 were 1.53 eV, 2.75 eV, and 1.98 eV, respectively. The VB potentials for PI, PI/TiO$_2$ and PI/TiO$_2$/Ag-0.07 were calculated as 2.02 V, 1.64 V and 1.58 V, and the conduction band (CB) potentials were -0.57 V, -1.32 V and -0.56 V. Based on the previously described band structures, a mechanism for photocatalytic degradation of TC by PI/TiO$_2$/Ag is proposed in Fig. 6g. Under simulated sunlight, the Ag QDs generated an intense electric field near their plasmon frequency, which excited the electrons of TiO$_2$ from the VB to the CB[41]. Subsequently, electron transfer from the CB of TiO$_2$ to Ag converted O$_2$ into $\cdot$O^{2-} (the superoxide anion radical) (-0.33 V vs. NHE). Nonetheless, the holes generated in the valence band of TiO$_2$ did not convert H$_2$O into $\cdot$OH (hydroxyl free radical) due to the negative potential of the TiO$_2$ valence band compared to the potential of $\cdot$OH/H$_2$O (2.34 V vs. NHE)[42,43]. Two protons, an e$^-$ and $\cdot$O^{2-} reacted to produce a small amount of $\cdot$OH. Importantly, the energy levels for Ag and the CB of TiO$_2$ were different. As a result, electrons migrated from the CB of TiO$_2$ to the Fermi level of Ag, which maintained electron/hole separation and accelerated the deterioration of TC[44]. The photocatalytic process can be described with the following equations:

$$PI/TiO_2/Ag + h\nu \rightarrow TiO_2(h^+) + Ag(e^-) \tag{2}$$

$$O_2 + e^- \rightarrow \cdot O^{2-} \tag{3}$$

$$\cdot O^{2-} + e^- + 2H^+ \rightarrow H_2O_2 \tag{4}$$

$$H_2O_2 + e^- \rightarrow OH + OH^- \tag{5}$$

$$\cdot O^{2-}/\cdot OH/h^+ + TC \rightarrow Products \tag{6}$$
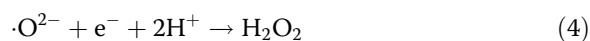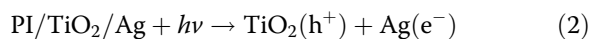
To provide intuitive verification of the active species involved in the photocatalytic mechanism described above, the efficiency of TC degradation by PI/TiO$_2$/Ag-0.07 was investigated with various scavengers. As displayed in Fig. 6h, the efficiency of TC degradation was reduced by the addition of different reactive scavengers. Specifically, the addition of 1 mM EDTA-2Na[45] and 4-hydroxy-TEMPO[46] as scavengers for h$^+$ and $\cdot$O^{2-}, respectively, resulted in substantial decreases in the rate of TC degradation. Only 21.8% and 26.8% of the TC was degraded, which were much lower than the degradation rates seen without scavengers (93.1%). This strong inhibition implied that both h$^+$ and $\cdot$O^{2-} were important reactive species, although h$^+$ had a slightly greater
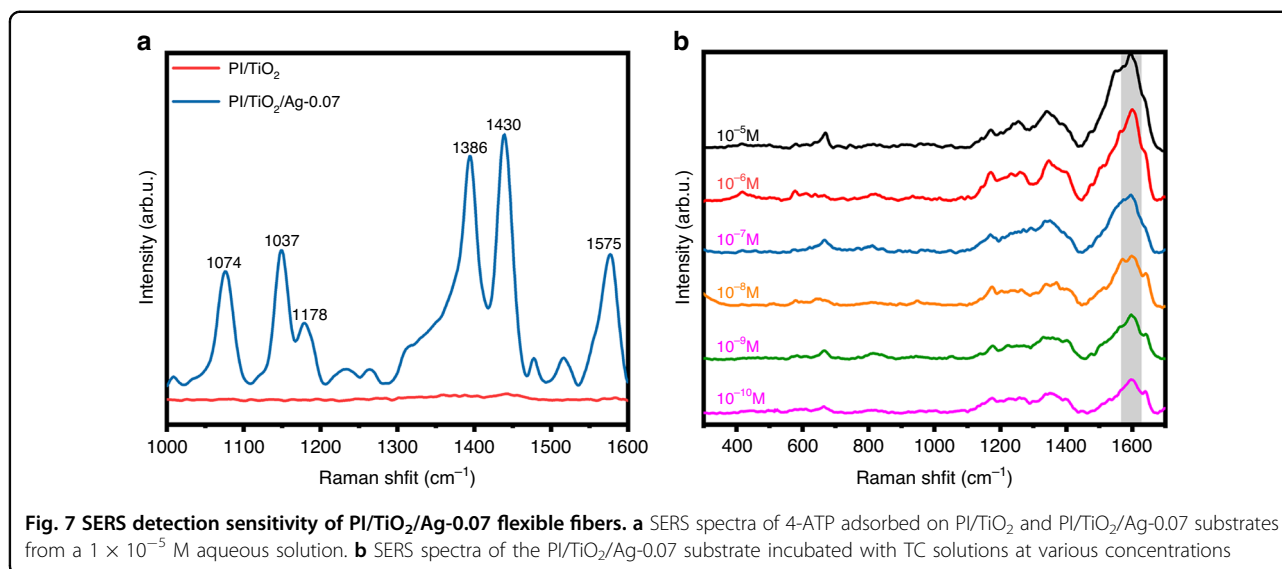
influence. Moreover, in using 1 mM IPA[47] as a scavenger for $\cdot$OH, the photocatalytic rate of TC degradation was reduced from 93.1% to 75.3%, indicating the significance of $\cdot$OH in the degradation of TC. These results were consistent with the photocatalytic mechanism.

SERS activity

As noted above, PI/TiO$_2$/Ag catalyzed photocatalytic degradation and enhanced SERS detection of the pollutants. As SERS substrates, PI/TiO$_2$ and PI/TiO$_2$/Ag-0.07 were utilized to detect 4-ATP in a 1×10^{-5} M solution to identify the better SERS substrate. As shown Fig. 7a, the peaks at 1137 cm^{-1}, 1386 cm^{-1}, and 1430 cm^{-1} corresponded to the "b2" vibrational modes $\nu_{C-C} + \nu_{C-S}$, β_{C-H}, and ν_{C-C}, respectively. Additionally, the peaks at 1074 cm^{-1}, 1178 cm^{-1}, and 1575 cm^{-1} represented the "a1" vibration modes attributed to $\nu_{C-C} + \nu_{C-S}$, β_{C-H}, and ν_{C-C}, respectively[48]. The peak intensity for 4-ATP enhanced with PI/TiO$_2$ was very weak. However, when PI/TiO$_2$/Ag-0.07 was applied, the intensity of the SERS signal was significantly enhanced, which indicated that PI/TiO$_2$/Ag enabled sensitive detection of 4-ATP. The enhancement originated from two factors: first, under irradiation, localized surface plasmon resonance (LSPR) of the Ag QDs formed a local electromagnetic field and accelerated charge transfer in PI/TiO$_2$/Ag; second, the Schottky barrier formed by the Ag QDs also facilitated charge transfer. The efficient charge transfer enhanced the SERS signal[49,50]. We then used the PI/TiO$_2$/Ag-0.07 substrate for SERS detection of TC. As shown in Fig. 7b, the SERS signal decreased gradually as the TC concentration was decreased, but even at a low concentration of 1×10^{-10} M, the PI/TiO$_2$/Ag-0.07 substrate still generated an appreciable SERS signal.

Conclusions

In summary, we employed a simple and effective strategy to fabricate novel PI/TiO$_2$/Ag organic−inorganic ternary flexible composite microfibers that exhibited both sensitive SERS detection and highly efficient photocatalytic degradation. The proportion of Ag QDs was a key factor influencing the photocatalytic and SERS performance of the fabricated samples. As the content of Ag was increased, the efficiency for photocatalytic degradation with PI/TiO$_2$/Ag initially increased and then decreased. The initial increase was attributed to the combined contributions of SPR and visible light absorption by Ag, as well as the Schottky barrier formed between Ag and TiO$_2$. The decreased photocatalytic degradation performance was ascribed to the excess Ag occupying the reactive sites. A photocatalytic degradation mechanism for PI/TiO$_2$/Ag was proposed and validated with free radical scavenging experiments. Among the samples, the PI/TiO$_2$/Ag-0.07

Fig. 7 SERS detection sensitivity of PI/TiO$_2$/Ag-0.07 flexible fibers. a SERS spectra of 4-ATP adsorbed on PI/TiO$_2$ and PI/TiO$_2$/Ag-0.07 substrates from a 1×10^{-5} M aqueous solution. **b** SERS spectra of the PI/TiO$_2$/Ag-0.07 substrate incubated with TC solutions at various concentrations

flexible microfibers exhibited the best photocatalytic performance, achieving degradation efficiencies of 93.1%, 95.5%, 100% and 100% for TC, MB, MO and Rh B, respectively. Additionally, the PI/TiO$_2$/Ag-0.07 flexible microfibers enabled sensitive SERS detection, as evidenced by the peaks observed even at a low TC concentration of 10^{-10} M. It is believed that these new perspectives for the design of innovative, highly efficient, and multifunctional organic−inorganic ternary flexible composite microfibers will contribute to advancements in energy conservation and environmental protection.

Experimental section
Materials

No additional purification was carried out on any of the materials before they were used. Pyromellitic dianhydride (PMDA), 4,4′-oxydianiline (4,4′-ODA), titanium, ascorbic acid, a solution of ethylenediamin etetraacetic acid (EDTA-2Na) and 4-hydroxy-TEMPO were purchased from Aladdin. AgNO$_3$ and hydrochloric acid solution (HCl) were obtained from Beijing Chemical Works. N,N-Dimethylformamide (DMF), isopropyl alcohol (IPA) and TC were purchased from Macklin.

Synthesis of PI nanofibers

4,4′-ODA (0.4 g) was added to 3.3 mL of DMF and dissolved by continuous stirring for 30 min. In an ice-water bath, 0.433 g of PMDA was added to the mixed solution in batches and vigorously stirred for 12 h. Subsequently, a light-yellow viscous solution (PAA) was obtained. The combined solution was then poure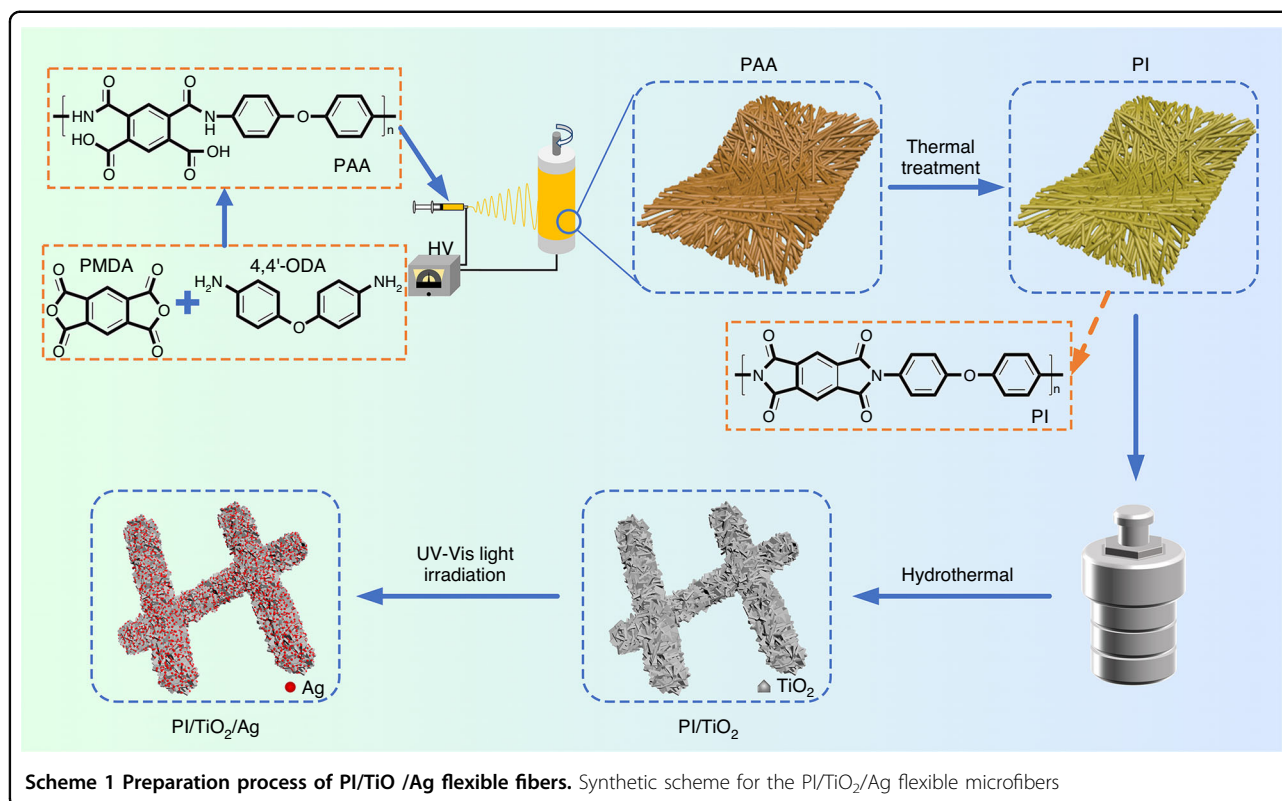d into a plastic syringe with a 3 mL capacity for electrospinning. Aluminum foil served as the collector, while a 12 kV electrical potential was applied with a 15 cm electrode spacing. Afterward, the PAA nanofibers were removed and placed into a muffle furnace, where they were heated to 300 °C at a rate of 2.5 °C/minute and maintained at this temperature for 2 h. Finally, the PI nanofibers were successfully prepared.

Synthesis of the PI/TiO$_2$ composite

To a vessel with a polytetrafluoroethylene liner, 0.045 g of titanium, 3 mL of 12 M HCl, and 33 mL of deionized water were added. Then, the PI nanofibers were soaked in this solution for 2 h. The autoclave vessel was put in the oven and maintained at 160 °C for 14 h. The obtained sample was repeatedly washed with deionized water and then dried in a 60 °C oven. The TiO$_2$ nanorod array was successfully "planted" on top of the brilliant yellow PI nanofiber membrane, and the PI/TiO$_2$ composite microfibers were created, as was evident from the layer of silver-gray that formed on the surface.

Synthesis of the PI/TiO$_2$/Ag composite

Ternary PI/TiO$_2$/Ag composite microfibers were created with electrospinning, a hydrothermal approach, and a photoreduction method (as shown in Scheme 1). The PI/TiO$_2$ composite nanofibers were irradiated with simulated sunlight from an Xe lamp for 1 h. Then, the PI/TiO$_2$ composite microfibers were immersed in 0.05, 0.07 and 0.09 M AgNO$_3$ solutions for 4 h. After drying under vacuum, the microfibers were again irradiated for 2 h to create the PI/TiO$_2$/Ag composite microfibers. The samples created with the various concentrations were designated PI/TiO$_2$/Ag-0.05, PI/TiO$_2$/Ag-0.07, and PI/TiO$_2$/Ag-0.09.

Scheme 1 Preparation process of PI/TiO /Ag flexible fibers. Synthetic scheme for the PI/TiO$_2$/Ag flexible microfibers

Characterization

KBr pellets were used to examine the FTIR spectra with a SHIMADZU FTIR-8400s spectrophotometer. A Bruker AXS D2 PHASER was employed to record XRD patterns with Cu Kα radiation. A NETZSCH STA 449F3 system was used to conduct TGA studies under air, with a heating rate of 10 °C/min up to 800 °C. SEM with a JSM-6701F system and TEM with a Tecnai F20 system equipped with EDX were used to analyze the morphologies and elemental distributions of the photocatalysts. A Micrometrics ASAP-2460 Surface Area and Porosimetry Analyzer was used to measure the BET-specific surface areas. A Thermo Fisher ESCALAB 250Xi system was used to obtain the XPS data. The PL spectra were obtained at room temperature with a Hitachi F-4700 spectrophotometer with an excitation wavelength of 350 nm. A CS310H electrochemical work-station was used to assess the electrochemical performance.

Photocatalytic degradation of TC

The rate of TC degradation under simulated sunlight was measured to assess the photocatalytic activities of PI, PI/TiO$_2$, and PI/TiO$_2$/Ag. The experimental process was as follows: to achieve adsorption-desorption equilibrium, a piece of the photocatalyst was soaked in a TC solution (5 mg/L) and maintained in darkness for 30 min. At 20-min intervals, the concentrations of TC were detected at 355 nm with a SHIMADZU UVmini-1240 spectrophotometer.

SERS measurements

The wavelength, power, exposure time and attenuation degree of the laser used for the SERS measurement were 514 nm, 15 mW/cm^2, 15 s, and 10%, respectively. For the detection of 4-ATP and TC (solution state), analyte solutions (in EtOH) of various concentrations were applied to mesoporous PI/TiO$_2$ and PI/TiO$_2$/Ag micro-fibers by drip-casting. After the sample was blown to a semidry state with an ear washing ball, the SERS signal was measured.

Author details
[1]School of Materials Science and Engineering, Changchun University of Science and Technology, 130022 Changchun, China. [2]College of Science, Changchun University, 130022 Changchun, China. [3]Key Laboratory of Functional Materials Physics and Chemistry of the Ministry of Education, Jilin Normal University, 130103 Changchun, China

Author contributions
B.Y.G. designed and completed the experiment and finished the original draft. Y.R.L., W.F., K.Y.L., and T.N.W. performed tests on the samples. Y.C.W., L.L.W., M.G., and Y.L. were involved in the analyses of the experimental results. M.B.W., S.Y., and D.L.H. revised the manuscript and gave reasonable proposals.

Competing interests
The authors declare no competing interests.

References

1. Hunge, Y. M., Yadav, A. A., Kang, S.-W. & Kim, H. Photocatalytic degradation of tetracycline antibiotics using hydrothermally synthesized two-dimensional molybdenum disulfide/titanium dioxide composites. *J. Colloid Interface Sci* **606**, 454–463 (2022).

2. Liu, L. et al. Treatment of industrial dye wastewater and pharmaceutical residue wastewater by advanced oxidation processes and its combination with nanocatalysts: a review. *J. Water Process.* **42**, 102122 (2021).

3. Ying, Y., Tang, Z. & Liu, Y. Material design, development, and trend for surface-enhanced Raman scattering substrates. *Nanoscale* **15**, 10860–10881 (2023).

4. Amruta, P., Sahu, J. N., Anil Kumar, P. & Prabir, G. Current perspective of nano-engineered metal oxide based photocatalysts in advanced oxidation processes for degradation of organic pollutants in wastewater. *Chem. Eng. Res. Des.* **190**, 667–686 (2023).

5. Huang, J. et al. Excellent visible light responsive photocatalytic behavior of N-doped TiO_2 toward decontamination of organic pollutants. *J. Hazard. Mater.* **403**, 123857 (2020).

6. Zheng, X. et al. Unidirectional/bidirectional electron transfer at the Au/TiO_2 interface operando tracked by SERS spectra from Au and TiO_2. *ACS Appl. Mater. Interfaces* **13**, 16498–16506 (2021).

7. Linsebigler, A. L., Lu, G. & Yates, J. T. Photocatalysis on TiO_2 surfaces: principles, mechanisms, and selected results. *Chem. Rev.* **95**, 735–758 (1995).

8. Kumar, A. et al. Recent advances in plasmonic photocatalysis based on TiO_2 and noble metal nanoparticles for energy conversion, environmental remediation, and organic synthesis. *Small.* **18**, 210638 (2021).

9. Cai, W. et al. TiO_2 Thickness-dependent charge transfer effect in p-aminothiophenol molecules chemisorbed on TiO_2/Ni substrates. *Appl. Surf. Sci.* **610**, 155573 (2022).

10. Anxin, J. et al. Aligned TiO_2 nanorod arrays decorated with closely interconnected Au/Ag nanoparticles: Near-infrared SERS active sensor for monitoring of antibiotic molecules in water. *Sensor Actuat. B: Chem.* **350**, 130848 (2021).

11. Shet, A. & Shetty, K. V. Photocatalytic degradation of phenol using Ag core-TiO_2 shell ($Ag@TiO_2$) nanoparticles under UV light irradiation. *Environ. Sci. Pollut. Res. Int.* **23**, 20055–20064 (2015).

12. Huang, Q. et al. Synthesis, characterization and application of TiO_2/Ag recyclable SERS substrates†. *Rsc Adv* **7**, 26704–26709 (2017).

13. Kumar, S., Lodhi, D. K. & Singh, J. P. Highly sensitive multifunctional recyclable Ag–TiO_2 nanorod SERS substrates for photocatalytic degradation and detection of dye molecules. *RSC Adv.* **6**, 45120–45126 (2016).

14. Qin, S., Cai, W., Tang, X. & Yang, L. Sensitively monitoring photodegradation process of organic dye molecules by surface-enhanced Raman spectroscopy based on $Fe_3O_4@SiO_2@TiO_2/Ag$ particle. *Analyst* **139**, 5509–5515 (2014).

15. Wang, S. et al. Preferentially oriented Ag-TiO_2 nanotube array film: An efficient visible-light-driven photocatalyst. *J. Hazard. Mater.* **399**, 123016 (2020).

16. Li, H. et al. Fabrication of pollutant-resistance SERS imprinted sensors based on $SiO_2@TiO_2@Ag$ composites for selective detection of pyrethroids in water. *J. Phys. Chem. Solids* **138**, 109254 (2020).

17. Xiao, Y. et al. The strategies of molecular architecture and modification of polyimide-based membranes for CO_2 removal from natural gas—a review. *Prog. Polym. Sci.* **34**, 561–580 (2009).

18. Liaw, D.-J. et al. Advanced polyimide materials: Syntheses, physical properties and applications. *Prog. Polym. Sci.* **37**, 907–974 (2012).

19. Dong, G. et al. TiO_2 nanoshell@polyimide nanofiber membrane prepared via a surface-alkaline-etching and in-situ complexation-hydrolysis strategy for advanced and safe LIB separator. *J. Membr. Sci.* **577**, 249–257 (2019).

20. Nah, C. et al. Characteristics of polyimide ultrafine fibers prepared through electrospinning. *Polym Int* **52**, 429–432 (2003).

21. Hu, Y. et al. Enhanced photocarrier separation in conjugated polymer engineered CdS for direct Z-scheme photocatalytic hydrogen evolution. *Appl Catal B-Environ* **260**, 118131 (2019).

22. Hu, L. et al. Direct electrospinning method for the construction of Z-scheme TiO_2/g-C_3N_4/RGO ternary heterojunction photocatalysts with remarkably ameliorated photocatalytic performance. *Chinese J. Catal* **40**, 458–469 (2019).

23. Zhou, J. et al. A (001) dominated conjugated polymer with high-performance of hydrogen evolution under solar light irradiation. *Chem. Commun.* **53**, 10536–10539 (2017).

24. Zhang, Y. et al. Construction of TiO_2/Ag_3PO_4 nanojunctions on carbon fiber cloth for photocatalytically removing various organic pollutants in static or flowing wastewater. *J. Colloid Interface Sci.* **571**, 213–221 (2020).

25. Xiong, H. et al. Controllable synthesis of mesoporous TiO_2 polymorphs with tunable crystal structure for enhanced photocatalytic H_2 production. *Adv. Energy Mater.* **9**, 1901634 (2019).

26. Shi, H. et al. Polyoxometalate/TiO_2/Ag composite nanofibers with enhanced photocatalytic performance under visible light. *Appl. Catal. B.* **221**, 280–289 (2017).

27. Zhou, J. K. et al. Synthesis of self-organized polycrystalline F-doped TiO_2 hollow microspheres and their photocatalytic activity under visible light. *J. Phys. Chem. C.* **112**, 5316–5321 (2008).

28. Zhiyuan, C. et al. Inverse opal structured Ag/TiO_2 plasmonic photocatalyst prepared by pulsed current deposition and its enhanced visible light photocatalytic activity. *J. Mater. Chem. A.* **2**, 824–832 (2013).

29. Guo, Q., Li, H., Zhang, Q. & Zhang, Y. Fabrication, characterization and mechanism of a novel Z-scheme Ag_3PO_4/NG/polyimide composite photocatalyst for microcystin-LR degradation. *Appl Catal B: Environ.* **229**, 192–203 (2018).

30. Meng, P., Heng, H., Sun, Y. & Liu, X. In situ polymerization synthesis of Z-scheme tungsten trioxide/polyimide photocatalyst with enhanced visible-light photocatalytic activity. *Appl. Surf. Sci.* **428**, 1130–1140 (2018).

31. Fu, J. et al. Hierarchical porous O-doped g-C_3N_4 with enhanced photocatalytic CO_2 reduction activity. *Small* **13**, 1603938 (2017).

32. Gai, L. et al. Controlled synthesis of nitrogen-doped binary and ternary TiO_2 nanostructures with enhanced visible-light catalytic activity. *J. Solid State Chem.* **199**, 271–279 (2013).

33. Dong, G. et al. Hierarchical mesoporous titania nanoshell encapsulated on polyimide nanofiber as flexible, highly reactive, energy saving and recyclable photocatalyst for water purification. *J. Clean. Prod.* **253**, 120021 (2020).

34. Gyawali, G. et al. Sonochemical synthesis of solar-light-driven Ag-$PbMoO_4$ photocatalyst. *J. Hazard. Mater.* **263**, 45–51 (2013).

35. Xiang, Q. et al. Au NAnoparticle Modified WO_3 nanorods with their enhanced properties for photocatalysis and gas sensing. *J. Phys. Chem. C* **114**, 2049–2055 (2010).

36. Linic, S., Christopher, P. & Ingram, D. B. Plasmonic-metal nanostructures for efficient conversion of solar to chemical energy. *Nat. Mater.* **10**, 911–921 (2011).

37. Chen, S. F. et al. Large scale photochemical synthesis of $M@TiO_2$ nanocomposites (M = Ag, Pd, Au, Pt) and their optical properties, CO oxidation performance, and antibacterial effect. *Nano Res.* **3**, 244–255 (2010).

38. Wang, M., Han, J., Xiong, H. & Guo, R. Yolk@Shell Nanoarchitecture of $Au@r$-GO/TiO_2 Hybrids as Powerful Visible Light Photocatalysts. *Langmuir.* **31**, 6220–6228 (2015).

39. Yang, S. et al. Monitoring the charge-transfer process in a Nd-doped semiconductor based on photoluminescence and SERS technology. *Light Sci. Appl.* **9**, 117 (2020).

40. Leng, W. H., Zhang, Z., Zhang, J. Q. & Cao, C. N. Investigation of the kinetics of a TiO_2 photoelectrocatalytic reaction involving charge transfer and recombination through surface states by electrochemical impedance spectroscopy. *J. Phys. Chem. B* **109**, 15008–15023 (2005).

41. Chen, D. et al. Synthesis and Ag-loading-density-dependent photocatalytic activity of $Ag@TiO_2$ hybrid nanocrystals. *Appl. Surf. Sci.* **284**, 921–929 (2013).

42. Chai, B. et al. In-situ synthesis of WO_3 nanoplates anchored on g-C_3N_4 Z-scheme photocatalysts for significantly enhanced photocatalytic activity. *Appl. Surf. Sci.* **448**, 1–8 (2018).

43. Zhu, B. et al. Fabrication and photocatalytic activity enhanced mechanism of direct Z-scheme g-C_3N_4/Ag_2WO_4 photocatalyst. *Appl. Surf. Sci.* **391**, 175–183 (2017).

44. Kumar, S. G. & Rao, K. S. R. K. Comparison of modification strategies towards enhanced charge carrier separation and photocatalytic degradation activity of metal oxide semiconductors (TiO_2, WO_3 and ZnO). *Appl. Surf. Sci.* **391**, 124–148 (2017).

45. Wang, Y. et al. Photocatalytic activity of N-TiO_2/O-doped N vacancy g-C_3N_4 and the intermediates toxicity evaluation under tetracycline hydrochloride and Cr (VI) coexistence environment. *Appl. Catal. B* **262**, 118308 (2020).

46. Chen, Y. et al. Naturally occurring sphalerite as a novel cost-effective photocatalyst for bacterial disinfection under visible light. *Environ. Sci. Technol.* **45**, 5689–5695 (2011).

47. Yu, F. et al. The preparation and properties of a g-C$_3$N$_4$/AgBr nanocomposite photocatalyst based on protonation pretreatment. *New J. Chem.* **39**, 1132–1138 (2014).

48. Cui, K. et al. Para-aminothiophenol radical reaction-functionalized gold nanoprobe for one-to-all detection of five reactive oxygen species in vivo. *Anal. Chem.* **90**, 12137–12144 (2018).

49. Hu, M. et al. Self-cleaning semiconductor heterojunction substrate: ultrasensitive detection and photocatalytic degradation of organic pollutants for environmental remediation. *Microsyst. Nanoeng.* **6**, 111 (2020).

50. Wu, T. et al. Self-sustainable and recyclable ternary Au@Cu$_2$O-Ag nanocomposites: application in ultrasensitive SERS detection and highly efficient photocatalysis of organic dyes under visible light. *Microsyst. Nanoeng.* **7**, 23 (2021).